Supplementary Information for

On-chip analogue signal processing using molybdenum disulfide reservoir computing

Authors

Yingyi Wen[1], Songwei Liu[1], Jingfang Pei[1], Zewen Kong[1], Yang Liu[1], Pengyu Liu[1], Xin Lu[2], Wenyu Cui[3], Xiaolong Chen[4], Teng Ma[3], Qiuqiang Kong[1], Steven Gao[1], Zegao Wang[2], Guohua Hu[1,*]

Affiliations

[1]Department of Electronic Engineering, The Chinese University of Hong Kong, Shatin, N. T., Hong Kong S. A. R., 999077, China

[2]College of Materials Science and Engineering, Sichuan University, Chengdu, 610065, China

[3]Department of Applied Physics, Hong Kong Polytechnic University, Hung Hom, Kowloon, Hong Kong S. A. R., 999077, China

[4]Department of Electrical and Electronic Engineering, Southern University of Science and Technology, Xueyuan Avenue, Shenzhen 518055, China

*Correspondence email: ghhu@ee.cuhk.edu.hk

This file contains:

Supplementary Figure S1-S14

Supplementary References

Supplementary Figures

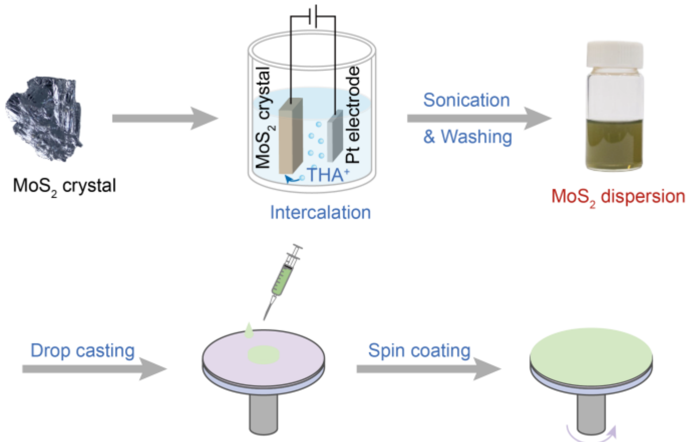

Figure S1. Exfoliation of MoS_2 and fabrication of MoS_2 thin film. The MoS_2 nanoflakes are obtained by electrochemical exfoliation of MoS_2 crystal. MoS_2 crystal (SPI Supplies) is cut into small strips and used as the cathode. Pt is the anode. The intercalation reaction is performed by applying 4 V bias between the Pt and MoS_2 electrodes in a N, N-Dimethylformamide (DMF) solution. The DMF solution has 5 mg/mL tetrahexylammonium bromide (THABr) and 20 mg/mL polyvinylpyrrolidone (PVP, molecular weight~40,000). The MoS_2 dispersion is obtained after intercalation, sonication, washing, and dispersion in isopropanol (IPA). The MoS_2 thin film is then deposited by spin coating of the MoS_2 dispersion at 2000 rpm on a wafer for multiple times (12 times in this work).

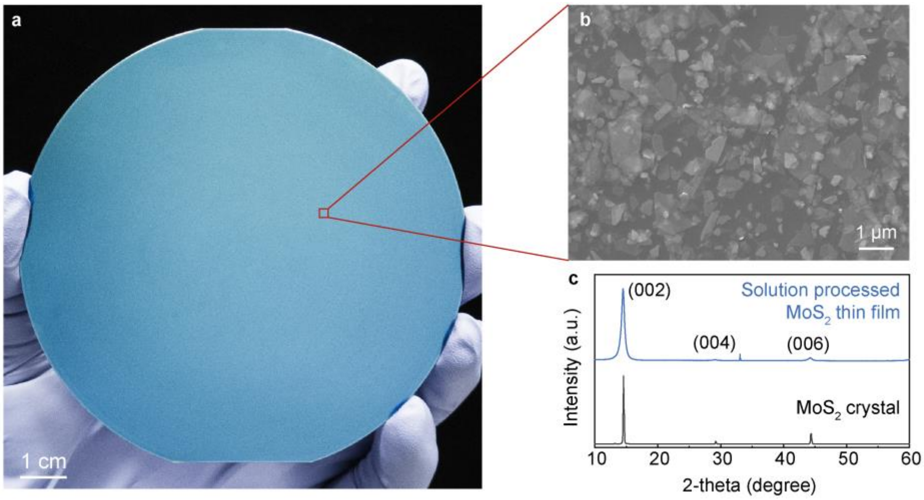

Figure S2. Solution processed MoS_2 thin film. (a) Photograph of a MoS_2 thin film deposited on a 4-inch SiO_2/Si wafer by spin coating of the MoS_2 dispersion. (b) SEM image of the deposited MoS_2 nanoflakes, showing a lateral dimension of ~0.5-1 μm for the typical nanoflakes. (c) XRD patterns of the MoS_2 thin film and the MoS_2 crystal. The presence of (002), (004), and (006) peaks suggests that the nanoflakes are well oriented along *c*-axis. The largely expanded (002) peak indicates that the MoS_2 nanoflakes are delaminated along *c*-axis.

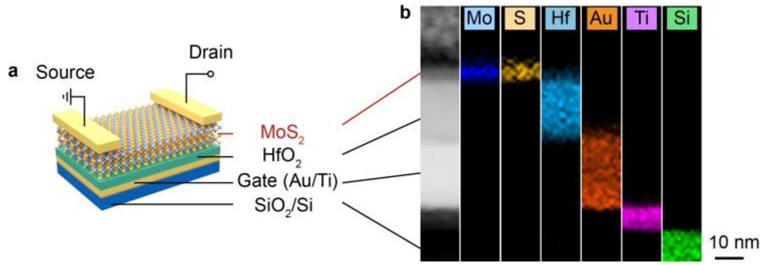

Figure S3. Device structure of the MoS_2 memory. (a) Vertical layered structure of the MoS_2 memory (replotted from Fig. 2b). Gate electrodes (15 nm Au / 5 nm Ti) are first defined by photolithography and thermal evaporation. Then 20 nm HfO_2 is grown on the wafer using atomic layer deposition (ALD). MoS_2 channel is deposited by spin coating and processed by dichloroethane solution of 5 mg/mL bis(trifluoromethane)sulfonimide (TFSI) at 70 °C. The channel is then patterned by oxygen reactive ion etching (RIE) using photoresist as the mask. The RIE is performed with a power of 200 W and an oxygen flow of 10 sccm for 40 s. Source and drain electrodes (15 nm Au / 5 nm Ti) are defined by another photolithography and thermal evaporation processes. (b) Cross-sectional high-resolution energy dispersive spectroscopy (EDS) mapping of the device vertical structure. The left is a cross-sectional high-angle annular dark-field scanning transmission electron microscopy (HAADF-STEM) image for reference. The EDS mapping clearly shows a layered structure of $MoS_2/HfO_2/Au/Ti/SiO_2$.

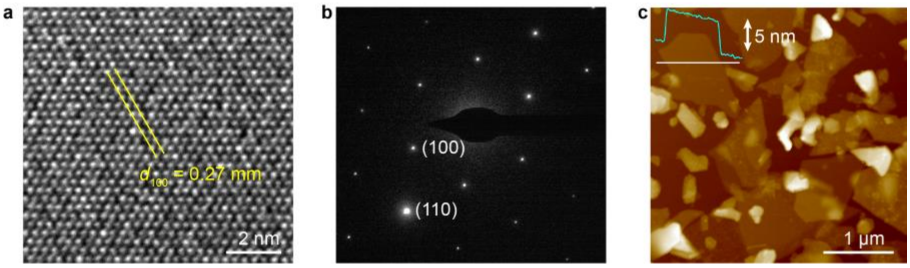

Figure S4. Solution-processed MoS_2 nanoflakes. (a) High-resolution transmission electron microscopy (TEM) image of a solution-processed MoS_2 nanoflake, showing a fringe distance of ~0.27 nm, corresponding to the lattice distance of MoS_2 in *a*-axis. (b) Selected-aera electron diffraction pattern (SEAD), showing hexagonal crystal structure of MoS_2 after exfoliation. (c) Atomic force microscopy (AFM) image of solution-processed MoS_2 nanoflakes, showing a lateral dimension of ~0.5-1 μm and a thickness of ~5 nm for the typical nanoflakes.

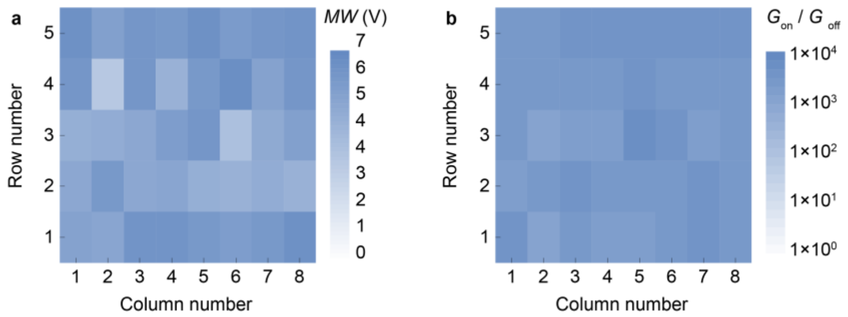

Figure S5. Device-to-device variation. Heatmap of (a) the memory window (*MW*) and (b) conductance on-off ratio (G_{on}/G_{off}) of the MoS_2 memory array extracted from transfer curves of 40 sampled devices shown in Fig. 2f. The device array shows good uniformity in performance, with *MW* of 3.35 ~ 6.58 V and G_{on}/G_{off} of $10^{3.01}$ ~ $10^{3.80}$.

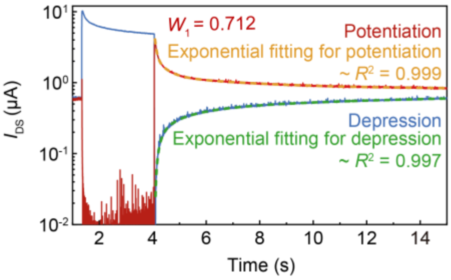

Figure S6. Fading characteristics of the MoS_2 memory. Relaxation of the MoS_2 memory in response to a single potentiation and depression pulse of -5 V and 5 V, respectively (replotted from Fig. 2k). The relaxation is read after setting V_G to 0V. V_{DS} is set as 2V during the whole measurement. The fading memory relaxation time constants are extracted by fitting the fading memory to a triple exponential function:

$$y = y_0 + A_1 \exp\left(-\frac{x-x_0}{t_1}\right) + A_2 \exp\left(-\frac{x-x_0}{t_2}\right) + A_3 \exp\left(-\frac{x-x_0}{t_3}\right),$$

where t_i is the relaxation time constant and A_i is the corresponding exponential coefficient. W_i denotes the weight of the relaxation time constant, and is calculated to quantify their contributions by $W_i = A_i / \sum A_i$.

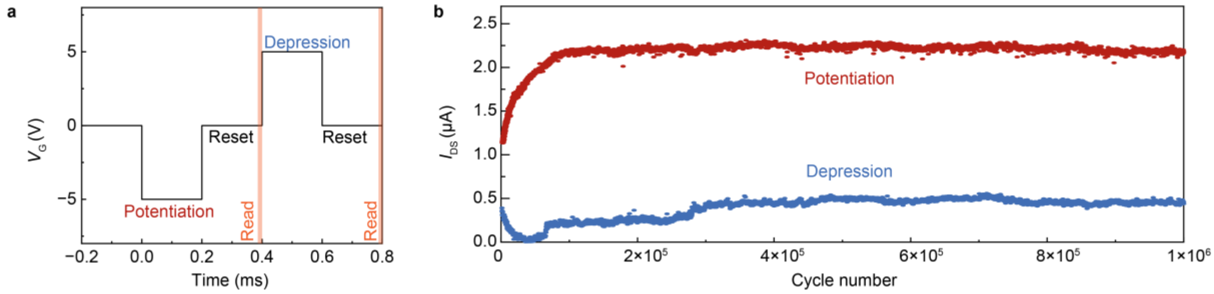

Figure S7. Endurance test of the MoS_2 memory. (a) Protocol for the endurance test. (b) Current outputs for over 1 million consecutive potentiation and depression pulses. A train of potentiation/depression pulses ($V_G = \pm 5$ V, 0.2 ms) are applied to the gate to program the state of the MoS_2 memory. A drain voltage of $V_{DS} = 0.7$ V is constantly supplied. After each pulse, current output is sampled after resetting the gate voltage ($V_G = 0$ V) for 0.2 ms. The high and low current outputs are shown as the red and blue dots. The device exhibits consistent behaviour after over 1 million pulsed operations.

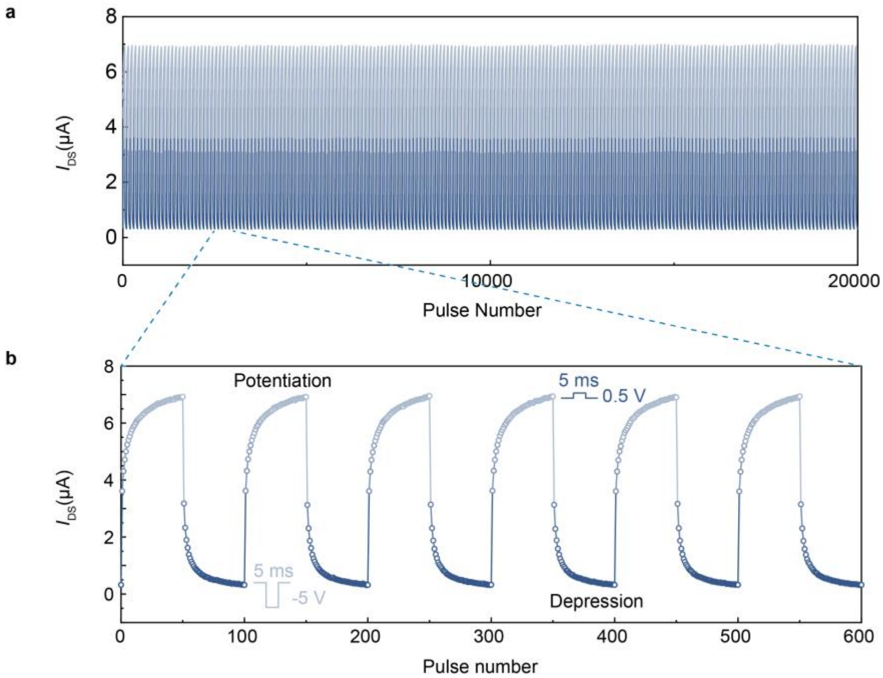

Figure S8. Cycle-to-cycle stability of the MoS_2 memory. (a) Device output characteristic of the MoS_2 memory during 200 consecutive cycles of potentiation and depression. Potentiation and depression are operated by applying negative (V_G = -5 V, 5 ms) and positive (V_G = 5 V, 5 ms) pulses, respectively, to the gate of MoS_2 memory. Current output is sampled after resetting the gate voltage (V_G = 0 V) for 0.2 ms. (b) Zoom-in device output characteristic for 6 consecutive potentiation/depression cycles. Standard deviations for the device outputs during the 200 consecutive potentiation/depression cycles are 0.025 and 0.009, respectively, proving a good cycle-to-cycle stability.

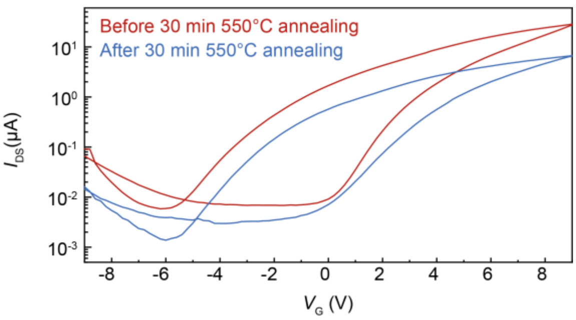

Figure S9. Transfer curves of the MoS_2 memory before and after annealing at 550°C. The annealing is conducted on a hotplate in a N_2 glove for 30 min to decompose the residual organic compounds from solution processing and device photolithographic fabrication[1,2]. The device after annealing still exhibits a memory effect with no large variation in the memory window, suggesting that the memory effect is not originated from the organic compounds. Otherwise, the device can lose the memory effect.

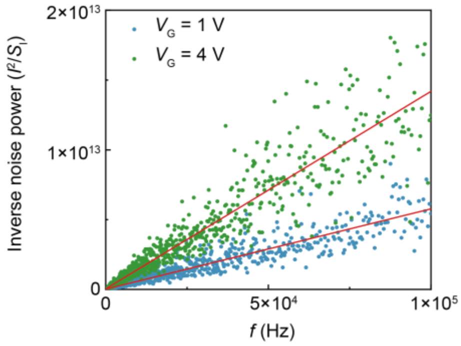

Figure S10. Inverse noise power versus frequency of the MoS_2 memory. The inverse noise power (I^2/S_I) as a function of frequency f under gate voltages V_G = 1 V and 4 V. The red lines are linear fits of the data points to extract noise amplitude A using $f\,(I^2/S_I = (1/A)f$ [3,4].

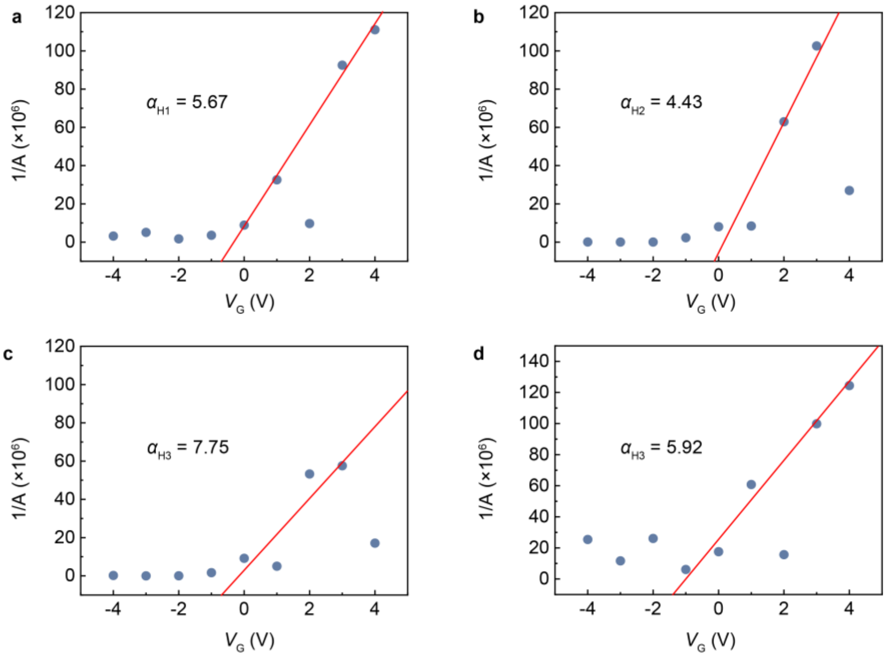

Figure S11. Inverse noise amplitude 1/*A* versus the gate voltage V_G of the MoS_2 memory. (a)-(d) 1/*A* versus V_G for four MoS_2 memory devices. The noise amplitude *A* is extracted by linear fitting the inverse noise power (I^2/S_I) as a function of frequency *f*. Hooge parameters α_H are extracted by linear fitting the 1/*A* as a function of V_G in the range V_G = 0~4 V using the formula $1/A = B|V_G - V_{th}|$, where $B = LWc_g/\alpha_H e$ [5,6]. *L*, *W*, c_g, *e* is channel length, channel width, gate capacitance per unit area, and elementary charge, respectively. V_{th} is the threshold voltage of the MoS_2 memory. The fitting is limited to the overdrive condition, where the device current is almost linear to V_G. The carrier concentration *N* can be approximated by a linear relation $N = (V_G - Vth)\ LWc_g\ /e$, which is used along with $A = (\alpha_H/N)$ to extract α_H. Anomalous points are eliminated for the fitting. The blue dots represent 1/*A* versus V_G, and the red lines denote the linear fitting of the data points. All noise data used for the fitting is collected with a drain voltage V_{DS} = 0.5 V. The large α_H indicates the existence of large amount of scattering centres in the MoS_2 memory.

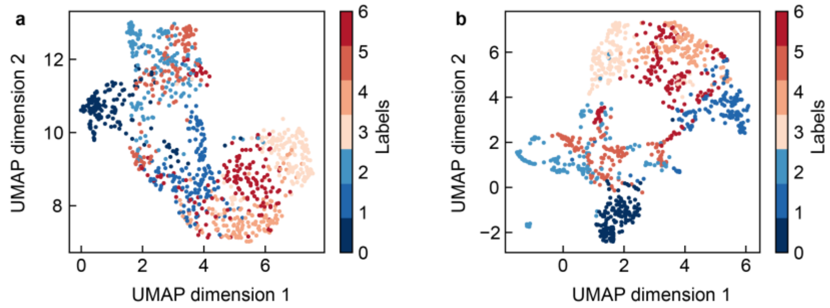

Figure S12. Universal manifold approximation and projection (UMAP) plots. UMAP plots of (a) the Myo sEMG dataset and (b) corresponding dataset after nonlinear mapping by the MoS_2 memory. UMAP is a method for dimensionality reduction. It uses a differentiable kernel to measure the similarity of the data points[7]. The result shows that the data points are more distinguishable after processing by the MoS_2 memory.

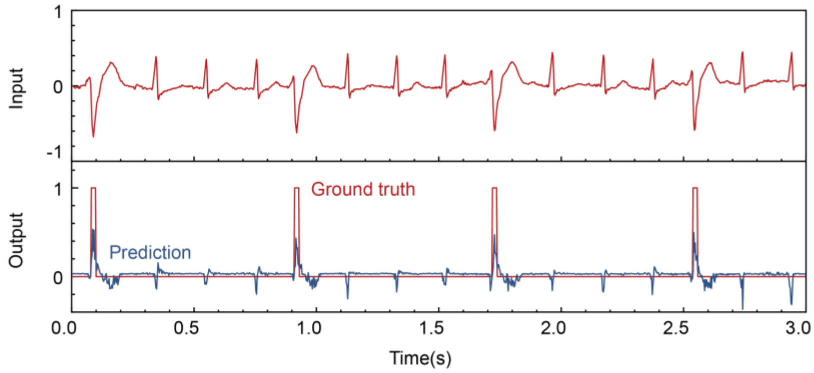

Figure S13. Arrhythmia detection using linear reservoir computing. The plot shows the result of the arrhythmia detection task in Fig. 5a using a reservoir computing with linear reservoir node, i.e. the MoS_2 memory, substituted by digital linear transformation. The reservoir computing shows much less filtering effect with both normal and arrythmia heartbeat poorly filtered.

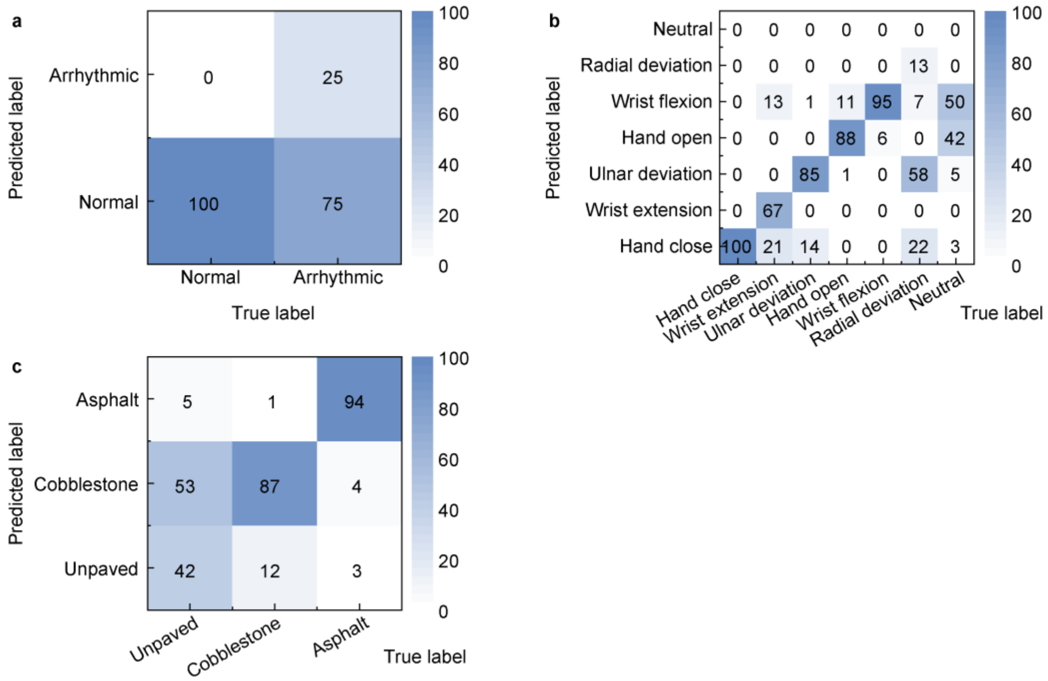

Figure S14. Classification of human and vehicle signals using linear reservoir computing. Confusion matrices of (a) the arrythmia detection, (b) hand gesture classification, and (c) road surface classification tasks using linear reservoir computing with digital linear transformation. The results show significantly worse performance when the MoS_2 memory nodes are substituted with linear reservoir nodes.

Supplementary References

1. Lu, Z., Yang, L. & Guo, Y. Thermal behavior and decomposition kinetics of six electrolyte salts by thermal analysis. *J. Power Sources* **156**, 555–559 (2006).

2. Jablonski, A. E., Lang, A. J. & Vyazovkin, S. Isoconversional kinetics of degradation of polyvinylpyrrolidone used as a matrix for ammonium nitrate stabilization. *Thermochim. Acta* **474**, 78–80 (2008).

3. Hooge, F. N. 1/*f* noise is no surface effect. *Phys. Lett. A* **29**, 139–140 (1969).

4. Hooge, F. N. 1/f noise sources. *IEEE Trans. Electron Devices* **41**, 1926–1935 (1994).

5. Hung, K. K., Ko, P. K., Hu, C. & Cheng, Y. C. A unified model for the flicker noise in metal-oxide-semiconductor field-effect transistors. 654–665 (1990).

6. Sangwan, V. K. *et al.* Low-Frequency Electronic Noise in Single-Layer MoS2 Transistors. *Nano Lett.* **13**, 4351–4355 (2013).

7. Healy, J. & McInnes, L. Uniform manifold approximation and projection. *Nat. Rev. Methods Prim.* **4**, 82 (2024).